arXiv:1208.0641v1 [math-ph] 3 Aug 2012

Structure analysis of single- and multi-frequency imaging functions in inverse scattering problems

Young Deuk Jo, Young Mi Kwon, Joo Young Huh, and Won-Kwang Park*

Abstract

In this literature, we carefully investigate the structure of single- and multi-frequency imaging functions, that are usually employed in inverse scattering problems. Based on patterns of the singular vectors of the Multi-Static Response (MSR) matrix, we establish a relationship between imaging functions and the Bessel function. This relationship indicates certain properties of imaging functions and the reason behind enhancement in the imaging performance by multiple frequencies. Several numerical simulations with a large amount of noisy data are performed in order to support our investigation.

1 Introduction

One of the main objective of the inverse scattering problem is to identify the characteristics of unknown targets from measured scattered field or far-field pattern. In research fields such as physics, medical science, and materials engineering, this is an interesting and important problem. Related works can be found in [2, 3, 8, 11, 12, 13, 29] and references therein. In order to solve this problem, various algorithms for finding the locations and/or shapes of targets have been accordingly developed.

In many research studies [2, 8, 11, 14, 18, 27], the shape reconstruction method is based on Newton-type iterative algorithms. However, for a successful shape reconstruction using these algorithms, the iterative procedure must begin with a good initial guess that is close to the unknown target because it highly depends on the initial guess; for more details, refer to [17, 27].

To finding a good initial guess, alternative non-iterative reconstruction algorithms have been developed, such at the MUltiple SIgnal Classification (MUSIC)-type algorithm [6, 24, 26], linear sampling method [9, 10], topological derivative strategy [4, 7, 19, 22, 23], and the multi-frequency based algorithm [3, 5, 20, 21, 25]. Among them, although the multi-frequency based algorithm has exhibited potential as a non-iterative imaging technique, a mathematical identification of its structure needs to be performed for its heuristical applications, which is the motivation behind.

In this paper, by intensively analyzing the structure of single- and multi-frequency imaging functions, we discover some properties of imaging functions and confirm the reason behind the enhancement in the imaging performance by applying multiple frequencies. In recent work [5], this fact was verified by the Statistical Hypothesis Testing but our approach is to find a relationship between imaging functions and Bessel functions of the first kind of the integer order.

This paper is organized as follows. In section 2, we briefly review the two-dimensional direct scattering problem, and an asymptotic expansion formula for far-field patterns, and introduce the imaging function introduced in [20]. In section 3, we analyze the single- and multi-frequency based imaging functions and discuss their properties. In section 4, we present several numerical experiments and discuss the effectiveness, robustness, and limitation of imaging functions. Finally, a brief conclusion is given in section 5.

---

*Department of Mathematics, Kookmin University, Seoul, 136-702, Korea. parkwk@kookmin.ac.kr

2 Review on imaging function

In this section, we survey the two-dimensional direct scattering problem and an imaging algorithm. A more detailed descussion can be found in [5, 6, 20, 21, 25].

2.1 Direct scattering problem and asymptotic expansion formula

Let Σ_m be a homogeneous inclusion with a small diameter ρ in the two-dimensional space $\mathbb{R}^2$. Throughout this paper, we assume that every Σ_m is expressed as

$$\Sigma_m = \mathbf{r}_m + \rho\mathcal{D}_m,$$

where $\mathbf{r}_m$ and ρ denote the location and size of Σ_m, respectively. Here, $\mathcal{D}_m$ is a simple connected smooth domain containing the origin.

Let ε_0 and μ_0 respectively denote the dielectric permittivity and magnetic permeability of $\mathbb{R}^2$. Similarly, we let ε_m and μ_m be those of Σ_m. For simplicity, let Σ be the collection of Σ_m, $m = 1, 2, \cdots, M$, and we define the following piecewise constants:

$$\varepsilon(\mathbf{r}) = \left\{ \begin{array}{ll} \varepsilon_m & \text{for} \quad \mathbf{r} \in \Sigma_m \\ \varepsilon_0 & \text{for} \quad \mathbf{r} \in \mathbb{R}^2 \backslash \overline{\Sigma} \end{array} \right. \quad \text{and} \quad \mu(\mathbf{r}) = \left\{ \begin{array}{ll} \mu_m & \text{for} \quad \mathbf{r} \in \Sigma_m \\ \mu_0 & \text{for} \quad \mathbf{r} \in \mathbb{R}^2 \backslash \overline{\Sigma}. \end{array} \right.$$

At a given frequency ω, let $u_{\text{tot}}(\mathbf{r}, \omega; l)$ be the time-harmonic total field that satisfies the Helmholtz equation

$$\nabla \cdot \left(\frac{1}{\mu(\mathbf{r})} \nabla u_{\text{tot}}(\mathbf{r}, \omega; l) \right) + \omega^2 \varepsilon(\mathbf{r}) u_{\text{tot}}(\mathbf{r}, \omega; l) = 0 \tag{1}$$

with transmission conditions

Let $u_{\text{inc}}(\mathbf{r}, \omega; l)$ be the solution of (1) without Σ. In this paper, we consider the following plane-wave illumination: for a vector $\mathbf{d}_l \in \mathfrak{C}^1$, $u_{\text{inc}}(\mathbf{r}, \omega; l) = \exp(j\omega \mathbf{d}_l \cdot \mathbf{r})$. Here, $\mathfrak{C}^1$ denotes a two-dimensional unit circle.

Generally, the total field u_{tot} can be divided into the incident field u_{inc} and the unknown scattered field u_{scat}, which satisfies the Sommerfeld radiation condition

$$\lim_{|\mathbf{r}| \to \infty} \sqrt{|\mathbf{r}|} \left(\frac{\partial u_{\text{scat}}(\mathbf{r}, \omega; l)}{\partial |\mathbf{r}|} - jk_0 u_{\text{scat}}(\mathbf{r}, \omega; l) \right) = 0, \quad k_0 = \omega \sqrt{\varepsilon_0 \mu_0}$$

uniformly in all directions $\hat{\mathbf{r}} = \frac{\mathbf{r}}{|\mathbf{r}|}$. As given in [6], u_{scat} can be written as the following asymptotic expansion formula in terms of ρ

$$\begin{aligned} u_{\text{scat}}(\mathbf{r}, \omega; l) = \rho^2 \sum_{m=1}^{M} \Big(& \nabla u_{\text{inc}}(\mathbf{r}_m, \omega; l) \cdot \mathbb{T}(\mathbf{r}_m) \cdot \nabla \Phi(\mathbf{r}_m, \mathbf{r}, \omega) \\ & + \omega^2 (\varepsilon - \varepsilon_0) u_{\text{inc}}(\mathbf{r}_m, \omega; l) \Phi(\mathbf{r}_m, \mathbf{r}, \omega) \Big) + o(\rho^2), \end{aligned} \tag{2}$$

where $o(\rho^2)$ is uniform in $\mathbf{r}_m \in \Sigma_m$ and $\mathbf{d}_l \in \mathfrak{C}^1$. Here $\Phi(\mathbf{r}_m, \mathbf{r}, \omega)$ is the two-dimensional time harmonic Green function (or fundamental solution to Helmholtz equation)

$$\Phi(\mathbf{r}_m, \mathbf{r}, \omega) = -\mu_0 \frac{j}{4} H_0^1(k_0 |\mathbf{r}_m - \mathbf{r}|),$$

where H_0^1 is the Hankel function of order zero and of the first kind.

The far-field pattern is defined as function $F(\hat{\mathbf{r}}, \mathbf{d})$ that satisfies

$$u_{\text{scat}}(\mathbf{r}, \omega; l) = \frac{\exp(jk_0 |\mathbf{r}|)}{\sqrt{|\mathbf{r}|}} F(\hat{\mathbf{r}}, \mathbf{d}) + o\left(\frac{1}{\sqrt{|\mathbf{r}|}} \right) \tag{3}$$

as $|\mathbf{r}| \longrightarrow \infty$ uniformly on $\hat{\mathbf{r}} = \frac{\mathbf{r}}{|\mathbf{r}|}$.

2.2 Introduction to imaging function

The imaging algorithm introduced in [20] used the structure of a singular vector of the Multi-Static Response (MSR) matrix $\mathbb{M} = (F_{pq}) = (F(\hat{\mathbf{r}}_p, \mathbf{d}_q))_{p,q=1}^N$. Note that by combining (2), (3), and the asymptotic behavior of the Hankel function, the far-field pattern F_{pq} with observation number p and incident wave number q can be represented as the asymptotic expansion formula (see [6] for instance)

$$F(\hat{\mathbf{r}}_p, \mathbf{d}_q) \approx \rho^2 \frac{k_0^2(1+j)}{4\sqrt{k_0\pi}} \sum_{m=1}^{M} \left(\frac{\varepsilon - \varepsilon_0}{\sqrt{\varepsilon_0\mu_0}} - \hat{\mathbf{r}}_p \cdot \mathbb{T}(\mathbf{r}_m) \cdot \mathbf{d}_q \right) \exp\left(jk_0(\mathbf{d}_q - \hat{\mathbf{r}}_p) \cdot \mathbf{r}_m \right). \tag{4}$$

Here $\mathbb{T}(\mathbf{r}_m)$ is a 2×2 symmetric matrix:

$$\mathbb{T}(\mathbf{r}_m) = \frac{2\mu_0}{\mu_m + \mu_0} \text{area}(\mathcal{D}_m)\mathbb{I}_2,$$

where $\mathbb{I}_n$ denotes the $n \times n$ identity matrix. For the sake of simplicity, we eliminate the constant $\frac{k_0^2(1+j)}{4\sqrt{k_0\pi}}$ in (4). Then, the incident and observation direction configurations are kept same, i.e., for each $\hat{\mathbf{r}}_p = -\mathbf{d}_p$, the pq-th element of the MSR matrix $\mathbb{M}$ is given by

$$F_{pq} = F(\hat{\mathbf{r}}_p, \mathbf{d}_q)\bigg|_{\hat{\mathbf{r}}_p = -\mathbf{d}_p} \approx \rho^2 \sum_{m=1}^{M} \left[\frac{\varepsilon_m - \varepsilon_0}{\sqrt{\varepsilon_0\mu_0}} + \frac{2\mu_0}{\mu_m + \mu_0} \text{area}(\mathcal{D}_m) \mathbf{d}_p \cdot \mathbf{d}_q \right] \exp\left(jk_0(\mathbf{d}_p + \mathbf{d}_q) \cdot \mathbf{r}_m \right),$$

where $\text{area}(\mathcal{D}_m)$ denotes the area of $\mathcal{D}_m$.

Based on the above representation of F_{pq}, we introduce a vector $\mathbf{D}(\mathbf{r};\omega) \in \mathbb{C}^{N\times 1}$ as

$$\mathbf{D}(\mathbf{r};\omega) := \begin{pmatrix} \mathbf{e}_1 \exp(jk_0\mathbf{d}_1 \cdot \mathbf{r}) \\ \mathbf{e}_2 \exp(jk_0\mathbf{d}_2 \cdot \mathbf{r}) \\ \vdots \\ \mathbf{e}_N \exp(jk_0\mathbf{d}_N \cdot \mathbf{r}) \end{pmatrix}, \quad \text{where} \quad \mathbf{e}_p = (1, \mathbf{d}_p)^T. \tag{5}$$

Then $\mathbb{M}$ can be decomposed as follows:

$$\mathbb{M} = \sum_{m=1}^{M} \mathbf{D}(\mathbf{r}_m;\omega) \begin{pmatrix} \dfrac{\varepsilon_m - \varepsilon_0}{\sqrt{\varepsilon_0\mu_0}} & 0 \\ 0 & \mathbb{T}(\mathbf{r}_m) \end{pmatrix} \mathbf{D}(\mathbf{r}_m;\omega)^T.$$

This decomposition leads us to introduce an imaging algorithm as follows. First, let us perform the Singular Value Decomposition (SVD) as follows:

$$\mathbb{M} = \mathbb{U}\mathbb{S}\overline{\mathbb{V}}^T = \sum_{m=1}^{M} \sigma_m(\omega)\mathbf{U}_m(\omega)\overline{\mathbf{V}}_m(\omega)^T, \tag{6}$$

where $\mathbf{U}_m$ and $\mathbf{V}_m$ are the left and right singular vectors, respectively. Then, by defining a normalized unit vector

$$\mathbf{W}(\mathbf{r};\omega) := \frac{\mathbf{D}(\mathbf{r};\omega)}{|\mathbf{D}(\mathbf{r};\omega)|}, \tag{7}$$

we can introduce an imaging function as follows (see [5, 20, 21, 25])

$$\mathbb{W}(\mathbf{r};\omega) := \left| \sum_{m=1}^{M} \left(\overline{\mathbf{W}}(\mathbf{r};\omega) \cdot \mathbf{U}_m(\omega) \right) \left(\overline{\mathbf{W}}(\mathbf{r};\omega) \cdot \overline{\mathbf{V}}_m(\omega) \right) \right| \tag{8}$$

3 Structure analysis of imaging function

3.1 Structure of imaging function (8)

We now determind the structure of imaging function (8). For this purpose, we recall some useful statements.

Lemma 3.1 ([5]). *A relation $A \sim B$ means that there exists a constant C such that $A = CB$. Then, for vectors $\mathbf{U}_m$ and $\mathbf{V}_m$ in (6) and $\mathbf{W}(\mathbf{r};\omega)$ in (7), the following relationship holds*

$$\mathbf{W}(\mathbf{r}_m;\omega) \sim \mathbf{U}_m(\omega) \quad \text{and} \quad \mathbf{W}(\mathbf{r}_m;\omega) \sim \overline{\mathbf{V}}_m(\omega).$$

Lemma 3.2 ([15]). *Let $\mathbf{d}, \mathbf{r} \in \mathbb{R}^2$, and $\omega > 0$; then*

$$\int_{\mathfrak{C}^1} \exp(j\omega\mathbf{d}\cdot\mathbf{r})dS(\mathbf{d}) = 2\pi J_0(\omega|\mathbf{r}|),$$

where $J_\nu(x)$ denotes the Bessel function of order ν of the first kind.

Subsequently, we can explore the structure of (8) as follows

Theorem 3.3. *If the number of incident and observation directions is sufficiently large, then the imaging function (8) can be represented as follows:*

$$\mathbb{W}(\mathbf{r};\omega) \sim \sum_{m=1}^{M} J_0^2(\omega|\mathbf{r}_m - \mathbf{r}|). \tag{9}$$

Proof. By hypothesis, we assume that N is sufficiently large. For simplicity, we set $\triangle\mathbf{d}_p := |\mathbf{d}_p - \mathbf{d}_{p-1}|$ for $p = 2, 3, \cdots, N$, and $\triangle\mathbf{d}_1 := |\mathbf{d}_1 - \mathbf{d}_N|$. $\triangle\mathbf{d}_q$ is defined analogously. Then, applying Lemmas 3.1 and 3.2 yields

$$\begin{aligned}\mathbb{W}(\mathbf{r};\omega) &= \left|\sum_{m=1}^{M}\Big(\overline{\mathbf{W}}(\mathbf{r};\omega)\cdot\mathbf{U}_m(\omega)\Big)\Big(\overline{\mathbf{W}}(\mathbf{r};\omega)\cdot\overline{\mathbf{V}}_m(\omega)\Big)\right|\\ &\sim \left|\sum_{m=1}^{M}\left(\sum_{p=1}^{N}\exp(j\omega\mathbf{d}_p\cdot(\mathbf{r}_m-\mathbf{r}))\frac{\triangle\mathbf{d}_p}{2\pi}\right)\left(\sum_{q=1}^{N}\exp(j\omega\mathbf{d}_q\cdot(\mathbf{r}_m-\mathbf{r}))\frac{\triangle\mathbf{d}_q}{2\pi}\right)\right| \\ &\approx \frac{1}{4\pi^2}\left|\sum_{m=1}^{M}\int_{\mathfrak{C}^1}\exp(j\omega\mathbf{d}\cdot(\mathbf{r}_m-\mathbf{r}))dS(\mathbf{d})\right|^2 = \sum_{m=1}^{M} J_0^2(\omega|\mathbf{r}_m-\mathbf{r}|).\end{aligned} \tag{10}$$

This completes the proof. □

Note that $J_0(x)$ has the maximum value 1 at $x = 0$. This is the reason why the map of $\mathbb{W}(\mathbf{r};\omega)$ plots magnitude 1 at $\mathbf{r} = \mathbf{r}_m \in \Sigma_m$. Moreover, due to the oscillating property of $J_0(x)$, Theorem 3.3 indicates why imaging function (8) plots unexpected replicas, as shown in Figure 1.

3.2 Reason behind enhancement in the imaging performance by applying multiple frequencies

According to the Theorem 3.3, the oscillating pattern of the Bessel function must be reduced or eliminated in order to improve the imaging performance. One way to do so is to apply the high-frequency $\omega = +\infty$ in theory. Another way is to apply several frequencies to the imaging function (8) as follows:

$$\mathbb{W}(\mathbf{r};S) := \frac{1}{S}\left|\sum_{s=1}^{S}\mathbb{W}(\mathbf{r};\omega_s)\right| = \frac{1}{S}\left|\sum_{s=1}^{S}\sum_{m=1}^{M}\Big(\overline{\mathbf{W}}(\mathbf{r};\omega_s)\cdot\mathbf{U}_m(\omega_s)\Big)\Big(\overline{\mathbf{W}}(\mathbf{r};\omega_s)\cdot\overline{\mathbf{V}}_m(\omega_s)\Big)\right|. \tag{11}$$

Several researches in [3, 5, 20, 21] have confirmed on the basis of Statistical Hypothesis Testing and numerical experiments that the multi-frequency imaging function (11) is an improved version of the single-frequency version (9). The reason for this is discussed as follows.

Theorem 3.4. *If ω_S and the number of incident and observation directions are sufficiently large enough, then the structure of the imaging function (11) is*

$$\begin{aligned}\mathbb{W}(\mathbf{r};S)\sim\Bigg|&\frac{\omega_S}{\omega_S-\omega_1}\bigg(J_0^2(\omega_S|\mathbf{r}_m-\mathbf{r}|)+J_1^2(\omega_S|\mathbf{r}_m-\mathbf{r}|)\bigg)\\&-\frac{\omega_1}{\omega_S-\omega_1}\bigg(J_0^2(\omega_1|\mathbf{r}_m-\mathbf{r}|)+J_1^2(\omega_1|\mathbf{r}_m-\mathbf{r}|)\bigg)\Bigg|.\end{aligned}\tag{12}$$

Proof. According to (10), we can observe that

$$\mathbb{W}(\mathbf{r};S)\approx\frac{1}{S}\left|\sum_{s=1}^{S}J_0^2(\omega_s|\mathbf{r}_m-\mathbf{r}|)\right|\approx\frac{1}{\omega_S-\omega_1}\left|\int_{\omega_1}^{\omega_S}J_0^2(\omega|\mathbf{r}_m-\mathbf{r}|)d\omega\right|.$$

Using this, we apply an indefinite integral formula of the Bessel function (see [28, page 35]):

$$\int J_0^2(x)=x\bigg(J_0^2(x)+J_1^2(x)\bigg)+\int J_1^2(x)dx$$

in addition to a change of variable $\omega|\mathbf{r}_m-\mathbf{r}|=x$. This yields

$$\begin{aligned}&\int_{\omega_1}^{\omega_S}J_0^2(\omega|\mathbf{r}_m-\mathbf{r}|)d\omega=\frac{1}{|\mathbf{r}_m-\mathbf{r}|}\int_{\omega_1|\mathbf{r}_m-\mathbf{r}|}^{\omega_S|\mathbf{r}_m-\mathbf{r}|}J_0^2(x)dx\\&\quad=\omega_S\bigg(J_0^2(\omega_S|\mathbf{r}_m-\mathbf{r}|)+J_1^2(\omega_S|\mathbf{r}_m-\mathbf{r}|)\bigg)-\omega_1\bigg(J_0^2(\omega_1|\mathbf{r}_m-\mathbf{r}|)+J_1^2(\omega_1|\mathbf{r}_m-\mathbf{r}|)\bigg)\\&\qquad+\int_{\omega_1}^{\omega_S}J_1^2(\omega|\mathbf{r}_m-\mathbf{r}|)d\omega.\end{aligned}$$

Now, we consider the upper bound of

$$\Lambda(|\mathbf{r}_m-\mathbf{r}|,\omega_1,\omega_S):=\int_{\omega_1}^{\omega_S}J_1^2(\omega|\mathbf{r}_m-\mathbf{r}|)d\omega.$$

Note that since $J_1(0)=0$, let us assume that $|\mathbf{r}_m-\mathbf{r}|\neq 0$ and $0<\omega_S|\mathbf{r}_m-\mathbf{r}|\ll\sqrt{2}$. Then applying asymptotic behavior

$$J_\nu(x)\approx\frac{1}{\Gamma(\nu+1)}\left(\frac{x}{2}\right)^\nu$$

and boundedness property $J_\nu(\omega|\mathbf{r}_m-\mathbf{r}|)\le\frac{1}{\sqrt{2}}$ yields

$$\begin{aligned}\int_{\omega_1}^{\omega_S}J_1^2(\omega|\mathbf{r}_m-\mathbf{r}|)d\omega&\le\frac{1}{\sqrt{2}}\int_{\omega_1}^{\omega_S}J_1(\omega|\mathbf{r}_m-\mathbf{r}|)d\omega\approx\frac{1}{\sqrt{2}}\int_{\omega_1|\mathbf{r}_m-\mathbf{r}|}^{\omega_S|\mathbf{r}_m-\mathbf{r}|}\frac{J_1(x)}{|\mathbf{r}_m-\mathbf{r}|}dx\\&=\frac{1}{2\sqrt{2}|\mathbf{r}_m-\mathbf{r}|}\int_{\omega_1|\mathbf{r}_m-\mathbf{r}|}^{\omega_S|\mathbf{r}_m-\mathbf{r}|}xdx=\frac{(\omega_S)^2-(\omega_1)^2}{4\sqrt{2}}|\mathbf{r}_m-\mathbf{r}|\\&<\frac{\omega_S}{4\sqrt{2}}\omega_S|\mathbf{r}_m-\mathbf{r}|\ll\frac{\omega_S}{4}=O(\omega_S).\end{aligned}$$

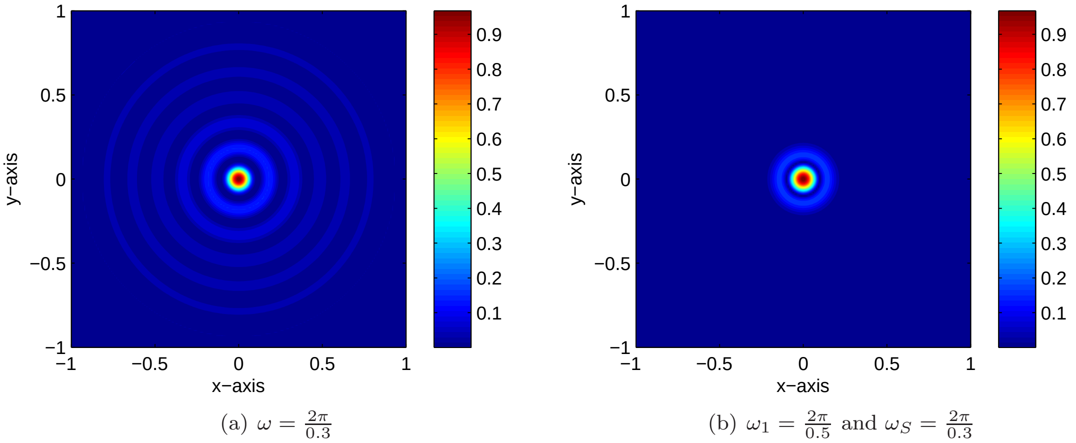

(a) $\omega = \frac{2\pi}{0.3}$

(b) $\omega_1 = \frac{2\pi}{0.5}$ and $\omega_S = \frac{2\pi}{0.3}$

Figure 1: (a) 2-D plot of (9) and (b) 2-D plot of (11) when $m = 1$ and $\mathbf{r}_m = \mathbf{0}$.

Now, assume that ω_S satisfies

$$\omega_S|\mathbf{r}_m - \mathbf{r}| \gg \sqrt{2} \quad \text{i.e.,} \quad |\mathbf{r}_m - \mathbf{r}| \gg \frac{\sqrt{2}}{\omega_S} > 0.$$

Then since

$$\int J_1(x)dx = -J_0(x),$$

we can obtain

$$\begin{aligned}\int_{\omega_1}^{\omega_S} J_1(\omega|\mathbf{r}_m - \mathbf{r}|)d\omega &= \int_{\omega_1|\mathbf{r}_m-\mathbf{r}|}^{\omega_S|\mathbf{r}_m-\mathbf{r}|} \frac{J_1(x)}{|\mathbf{r}_m - \mathbf{r}|}dx = \frac{1}{|\mathbf{r}_m - \mathbf{r}|}\Big[-J_0(x)\Big]_{\omega_1|\mathbf{r}_m-\mathbf{r}|}^{\omega_S|\mathbf{r}_m-\mathbf{r}|} \\ &= \frac{1}{|\mathbf{r}_m - \mathbf{r}|}\Big(J_0(\omega_1|\mathbf{r}_m - \mathbf{r}|) - J_0(\omega_S|\mathbf{r}_m - \mathbf{r}|)\Big) \\ &\le \frac{2}{|\mathbf{r}_m - \mathbf{r}|} \ll \sqrt{2}\omega_S.\end{aligned}$$

Therefore, the term $\Lambda(|\mathbf{r}_m - \mathbf{r}|, \omega_1, \omega_S)$ can be disregarded because

$$\Bigg|\frac{\omega_S}{\omega_S - \omega_1}\Big(J_0^2(\omega_S|\mathbf{r}_m - \mathbf{r}|) + J_1^2(\omega_S|\mathbf{r}_m - \mathbf{r}|)\Big) \\ - \frac{\omega_1}{\omega_S - \omega_1}\Big(J_0^2(\omega_1|\mathbf{r}_m - \mathbf{r}|) + J_1^2(\omega_1|\mathbf{r}_m - \mathbf{r}|)\Big)\Bigg| = O(\omega_S)$$

and $\Lambda(|\mathbf{r}_m - \mathbf{r}|, \omega_1, \omega_S) \ll O(\omega_S)$. Hence we can obtain (12). This completes the proof. □

The graph for (12) is shown in Figure 1. This graph shows that (11) yields better images owing to less oscillation than (9) does. This result indicates why a multi-frequency based imaging function offers better results than a single-frequency based one.

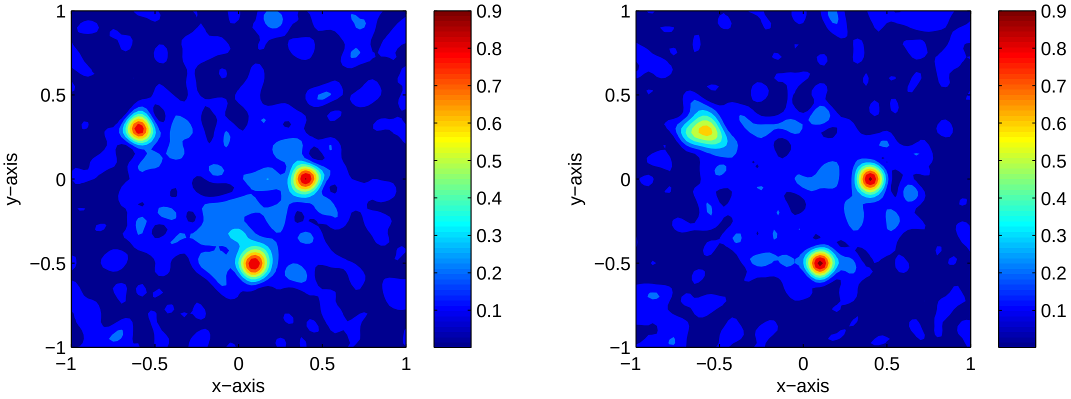

(a) same material property (b) different material property

Figure 2: Maps of $\mathbb{W}(\mathbf{r}; 10)$.

4 Numerical experiments and discussions

In this section, we describe the numerical experiments we conducted to validate our analysis. For this purpose, we choose a set of three different small disks Σ_m. The common radii ρ of Σ_m are set to 0.1, and parameters ε_0 and μ_0 are chosen as 1. Locations $\mathbf{r}_m$ of Σ_m are selected as

$$\mathbf{r}_1 = (0.4, 0), \quad \mathbf{r}_2 = (-0.6, 0.3), \quad \text{and} \quad \mathbf{r}_3 = (0.1, -0.5).$$

For a given wavelength λ_s, each frequency is selected as $\omega_s = \frac{2\pi}{\lambda_s}$, for $s = 1, 2, \cdots, S$. Note that all the wavelengthes λ_s are uniformly distributed in the interval $[\lambda_1, \lambda_S]$. The observation directions $\mathbf{d}_p \in S^1$ are selected as

$$\mathbf{d}_p = \left(\cos\frac{2\pi p}{N}, \sin\frac{2\pi p}{N}\right) \quad \text{for} \quad p = 1, 2, \cdots, N.$$

The incident directions $\mathbf{d}_q \in S^1$ are selected analogously.

In all the examples, a white Gaussian noise with 10 dB signal-to-noise ratio (SNR) is added to the unperturbed data in order to exhibit the robustness of the proposed algorithm via the MATLAB command *awgn*. In order to obtain the number of nonzero singular values M for each frequency ω_s, a 0.01-threshold scheme is adopted (see [24, 26]). The search domain Ω is selected as a square $\Omega = [-1, 1] \times [-1, 1]$.

Figure 2 shows the map of $\mathbb{W}(\mathbf{r}; 10)$ via the MSR matrix $\mathbb{M}$ for $N = 20$ and $S = 10$ and different frequencies with $\lambda_1 = 0.5$ and $\lambda_S = 0.3$. On the left-hand side of Figure 2, we set the same material properties $\varepsilon_m \equiv 5$ and $\mu_m \equiv 5$, $m = 1, 2, 3$. As expected, locations of Σ_m can be clearly identified. On the right-hand side of Figure 2, we set different material properties $\varepsilon_1 = \mu_1 = 5$, $\varepsilon_2 = \mu_2 = 2$, and $\varepsilon_3 = \mu_3 = 7$. Note that due to the small values of ε_2 and μ_2, the map of $\mathbb{W}(\mathbf{r}; 10)$ plots a small magnitude at $_2$ but the locations of all Σ_m are well identified.

Figure 3 shows the influence of the number of applied frequencies S. As we discussed in section 3, increasing S yields a more accurate image. Note that applying an infinite number of S would yield good results in theory, but in this experiment, $S = 10$ is sufficient for obtaining a good result.

Based on the recent work [20], the proposed algorithm can be applied to imaging of extended, crack-like electromagnetic inclusion(s) Γ with a supporting curve γ and a small thickness h. However, note that even a sufficiently large number of N and S applied to obtain a good image of

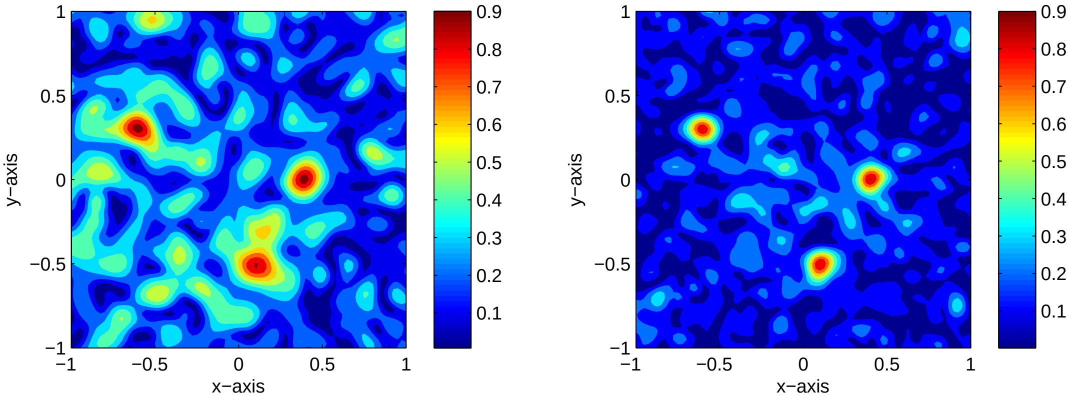

(a) $S = 1$

(b) $S = 3$

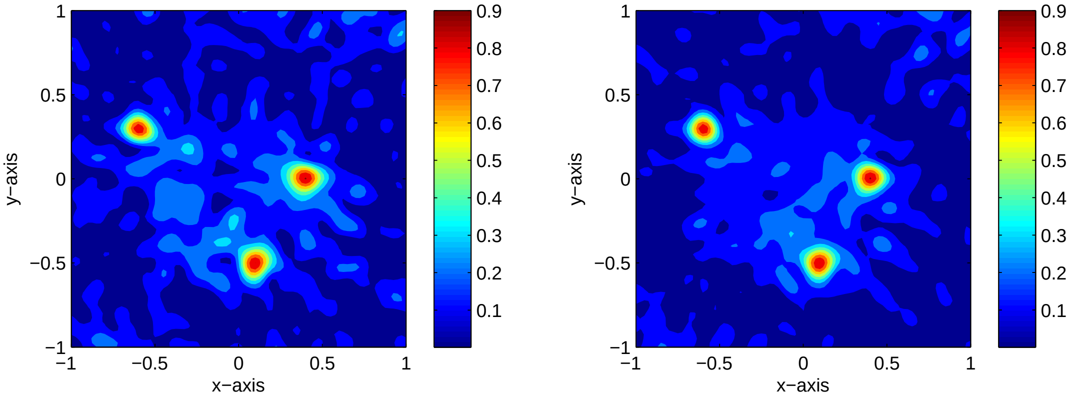

(c) $S = 7$

(d) $S = 20$

Figure 3: Maps of $\mathbb{W}(\mathbf{r}; S)$ with (a) $S = 1$ (b) $S = 3$ (c) $S = 7$ and (d) $S = 20$.

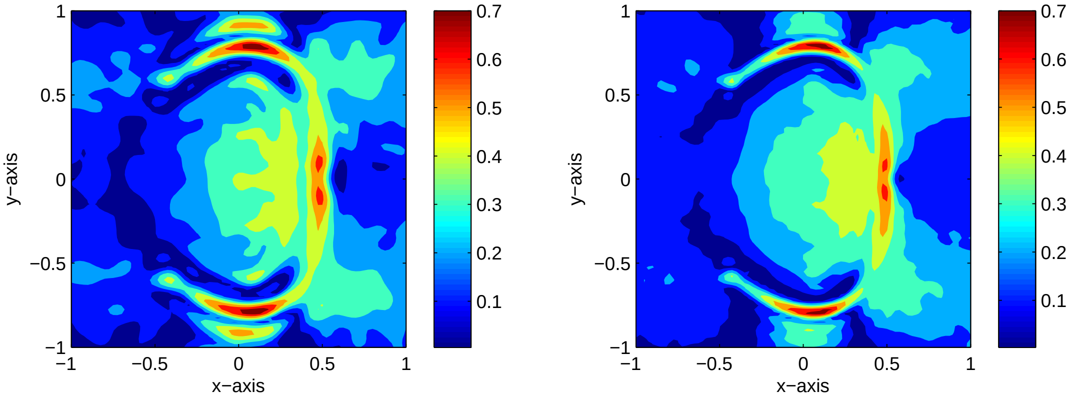

(a) $N = 48$ and $S = 10$

(b) $N = 64$ and $S = 24$

Figure 4: Maps of $\mathbb{W}(\mathbf{r}; S)$.

a complex-shaped thin inclusion using the proposed algorithm can occasionally yield poor results (see Figure 4). Furthermore, note that the elements of $\mathbb{M}$ are expressed as written by

$$F(\mathbf{d}_p, \mathbf{d}_q) \sim \sum_{m=1}^{M} \left[\frac{\varepsilon - \varepsilon_0}{\sqrt{\varepsilon_0 \mu_0}} + 2\left(\frac{1}{\mu} - \frac{1}{\mu_0}\right) \mathbf{d}_p \cdot \mathbf{t}(\mathbf{r}_m) \mathbf{d}_q \cdot \mathbf{t}(\mathbf{r}_m) \right.$$
$$\left. + 2\left(\frac{1}{\mu_0} - \frac{\mu}{\mu_0^2}\right) \mathbf{d}_p \cdot \mathbf{n}(\mathbf{r}_m) \mathbf{d}_q \cdot \mathbf{n}(\mathbf{r}_m) \right] \exp\Big(jk_0(\mathbf{d}_p + \mathbf{d}_q) \cdot \mathbf{r}_m\Big).$$

Therefore, $\mathbf{e}_p$ in (5) must be a linear combination of a unit tangential vector $\mathbf{t}(\mathbf{r}_m)$ and a normal vector $\mathbf{n}(\mathbf{r}_m)$ at $\mathbf{r} \in \gamma$. If we have *a priori* information of $\mathbf{t}(\mathbf{r}_m)$ and $\mathbf{n}(\mathbf{r}_m)$, we can obtain a good result. However, because this is not the case, it is difficult to obtain a good result. This is further explained in detail in [26, Section 4.3.1].

5 Conclusion

Using an integral representation formula and an indefinite integral of the Bessel function, we determined the structure of single and multiple electromagnetic imaging functions. Because of the oscillation aspect of the Bessel function, we confirmed the reason behind the improved imaging performance by successfully applying high and multiple frequencies.

Recent works [20, 21, 25] have shown that the proposed algorithm can be applied to limited-view inverse scattering problems. In order to determine the structure of imaging functions, the integration in Lemma 3.2 on the subset of a unit circle must be evaluated; however, this evaluation is very difficult to perform. Therefore, identifying the imaging function stucture in the limited-view problem will prove to be an interesting research topic. Moreover, in the imaging of crack-like inclusions, estimating unit tangential and normal vectors on such an inclusion and yielding relatively good results will be an interesting work.

Finally, we considered the imaging function for penetrable electromagnetic inclusions but it will be applied to the perfectly conducting inclusion(s) directly. Extension to the perfectly conducting target will be a forthcoming work. We further believe that the proposed strategy can be extended to a three-dimensional problem.

acknowledgments

W.-K. Park would like to thank Habib Ammari for introducing [3] and many valuable advices. This work was supported by the research program of Kookmin University in Korea, the Basic Science Research Program through the National Research Foundation of Korea (NRF) funded by the Ministry of Education, Science and Technology (No. 2012-0003207), and the WCU(World Class University) program through the National Research Foundation of Korea(NRF) funded by the Ministry of Education, Science and Technology R31-10049.

References

[1] M. Abramowitz and I. A. Stegun, *Handbook of Mathematical Functions, with Formulas, Graphs, and Mathematical Tables* (Dover, New York, 1996).

[2] D. Álvarez, O. Dorn, N. Irishina, and M. Moscoso, J. Comput. Phys., **228**, 5710 (2009).

[3] H. Ammari, *Mathematical Modeling in Biomedical Imaging II: Optical, Ultrasound, and Opto-Acoustic Tomographies*, Lecture Notes in Mathematics, **2035** (Springer-Verlag, Berlin, 2011).

[4] H. Ammari, J. Garnier, V. Jugnon, and H. Kang, SIAM J. Control. Optim., **50**, 48 (2012).

[5] H. Ammari, J. Garnier, H. Kang, W.-K. Park, and K. Sølna, SIAM J. Appl. Math., **71**, 68 (2011).

[6] H. Ammari and H. Kang, *Reconstruction of Small Inhomogeneities from Boundary Measurements, Lecture Notes in Mathematics*, **1846** (Springer-Verlag, Berlin, 2004).

[7] H. Ammari, H. Kang, H. Lee and W.-K. Park, SIAM J. Sci. Comput., **32**, 894 (2010).

[8] X. Chen, J. Electromagn. Waves Appl., **23** 1397 (2009).

[9] M. Cheney, Inverse Problems, **17**, 591 (2001).

[10] D. Colton, H. Haddar and P. Monk, SIAM J. Sci. Comput., **24**, 719 (2002).

[11] F. Delbary, K. Erhard, R. Kress, R. Potthast and J. Schulz, Inverse Problems, **24**, 015002 (2008).

[12] M. Donelli, Prog. Electromagn. Res. M, **19**, 173 (2011).

[13] M. Donelli, I. J. Craddock, D. Gibbins and M. Sarafianou, Prog. Electromagn. Res. M, **18**, 179 (2011).

[14] O. Dorn and D. Lesselier, Inverse Problems, **22**, R67 (2006).

[15] R. Griesmaier, Inverse Problems, **27**, 085005 (2011).

[16] A. Kirsch and S. Ritter, Inverse Problems, **16**, 89 (2000).

[17] O. Kwon, J. K. Seo, and J.-R. Yoon, Commun. Pur. Appl. Math., **55**, 1 (2002).

[18] D. Lesselier and Duchene B., Prog. Electromagn. Res., **5**, 351 (1991).

[19] Y.-K. Ma, P.-S. Kim and W.-K. Park, Prog. Electromagn. Res., **122** 311 (2012).

[20] W.-K. Park, Prog. Electromagn. Res., **106**, 225 (2010).

[21] W.-K. Park, Inverse Problems, **26**, 074008 (2010).

[22] W.-K. Park, Prog. Electromagn. Res., **110**, 237 (2010).

[23] W.-K. Park, J. Comput. Phys., **231**, 1426 (2012).

[24] W.-K. Park and D. Lesselier, J. Comput. Phys., **228**, 8093 (2009).

[25] W.-K. Park and D. Lesselier, Waves Random Complex Media, **22**, 3 (2012).

[26] W.-K. Park and D. Lesselier, Inverse Problems, **25**, 075002 (2009).

[27] W.-K. Park and D. Lesselier, Inverse Problems, **25**, 085010 (2009).

[28] W. Rosenheinrich, `http://www.fh-jena.de/~rsh/Forschung/Stoer/besint.pdf`.

[29] Y. Zhou, Prog. Electromagn. Res. Lett., **19**, 57 (2010).